Microstrip Ferrite Circulator Design With Control of Magnetization Distribution

Laila Marzall, *Student Member, IEEE*, Dimitra Psychogiou, *Senior Member, IEEE*,
and Zoya Popović, *Fellow, IEEE*

Abstract—This article presents a study of the impact of different external magnetic bias field (MBF) distributions on Y-junction microstrip ferrite circulator performance. By using magnetostatic, full-wave, and circuit commercial simulation tools for a circular ferrite disk, several permanent magnet (PM) configurations are investigated for unsaturated and nonuniform bias conditions. Eigenmode simulations are used to analyze the circulator bandwidth over a range of MBF intensities. We show in simulations and experiments that different bias conditions can result in an operating frequency range from 1.5 to 7 GHz using the same 9.7-mm-diameter commercial ferrite disk resonator.

Index Terms—Eigenmode simulation, ferrites, nonuniform magnetic bias field (MBF), permanent magnets (PMs), Y-junction circulators.

I. INTRODUCTION

CIRCULATORS have been in use for a long time in microwave systems to isolate a receiver from a transmitter in full-duplex operation and remain essential components for transmit/receive front ends [1], [2]. Externally biased ferrite circulators were first examined in the 1950s (see [3]). The theoretical framework for circulator design was established in the 1960s [4], [5], and a dyadic Green's function-based analysis is discussed in, e.g., [6]. Stripline circulators were first treated in the early 1960s (see [4], [5], [7], [8]). Wideband designs with over 50% fractional bandwidth using different disk shapes are discussed in [9]. A ferrite circulator integrated with a low-temperature cofired ceramic (LTCC) stripline circuit is simulated using full-wave numerical tools in [10]. Microstrip circulator design is presented in [11] and [12] with broadband approaches discussed in [13], including antenna-circulator integration in [14] and [15]. A 7-GHz microstrip circulator in an LTCC substrate using ferrite tape is shown in [16]. Thin-film devices have also been demonstrated, e.g., in [17].

Fig. 1 shows the geometry of a microstrip circulator, where permanent magnets (PMs) generate the desired magnetic bias
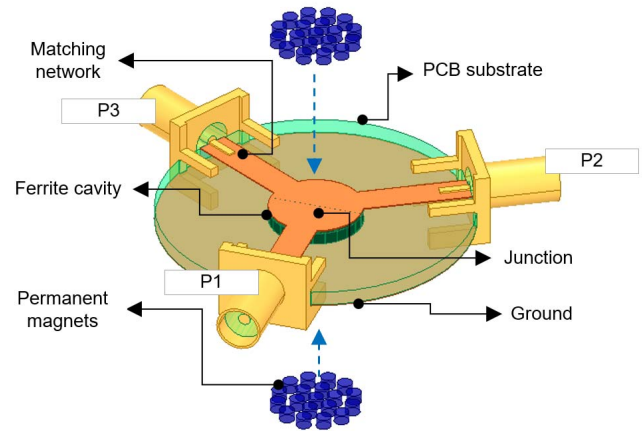
Fig. 1. Overall geometry of a Y-junction ferrite circulator. The PMs produce an MBF in the ferrite. A wave input at port P1 is transmitted to P2 with low insertion loss, whereas P3 is isolated (counterclockwise circulation) or transmitted to P3 with P2 isolated (clockwise), depending on the resonator mode and direction of MBF. The microstrip junction is above the ferrite disk and the PMs (shown here as an array) are placed immediately above and below the disk.

field (MBF) within the ferrite disk, producing nonreciprocal behavior. However, the MBF is generally not constant throughout the disk, and the strength of the magnets may not be sufficient to fully saturate the ferrite. Unsaturated ferrites are discussed in [18], and partially magnetized ones are studied in [19] and [20]. The effect of demagnetization is further discussed in [6], [21], and [22]. A reduction in bandwidth due to a nonuniform magnetic field is detailed in [23] and validated at X-band. In [24], a comparison is performed between a computed nonuniform MBF and full-wave electromagnetically simulated uniform one (using Ansys HFSS), showing that nonuniformity should be considered.

In traditional designs, the magnetic bias is produced by a pair of cylindrical PMs, in general larger than the ferrite disk. The analysis presented here allows for more complex 3-D configurations, such as the small-magnet arrays shown in Fig. 1, which enables the same ferrite resonator to be used for circulators at frequencies across more than two octaves.

Recently, there has been an increasing interest in self-biased ferrite materials for circulator design, which does not require an external source for biasing, leading to the potential integration with amplifiers in monolithic microwave integrated circuits (MMICs) for RF front ends [25], [26]. In such devices, the material properties are generally nonuniform, and the

disk operates in unsaturated conditions. This gives further motivation to investigate the impacts of nonuniform biasing and nonsaturated magnetization on circulator performance.

Most high-end electromagnetic (EM) simulators, such as HFSS, use Polder's model to calculate the ferrite permeability tensor $[\mu]$. The model is not intended for analysis of weakly biased ferrites. Even in unsaturated regions, individual domains (micrometer in size) are always saturated at the saturation magnetization M_s. However, at the millimeter scale of RF EM modes in the ferrite, the net magnetization can vary from point to point. Thus, the linewidth measured in saturation is not a good representation for nonsaturated regions, and the Polder model used in HFSS is inaccurate. In order to best use the full-wave analysis tool, we recognize this limitation and set the external MBF at a lower value than M_s where the ferrite is not fully saturated. With this approximation, we find that the analysis agrees well with measurements while allowing us to take advantage of the power of full-wave simulations of a ferrite disk with matching networks and the real magnetic bias structure.

In this article, full-wave EM and magnetostatic cosimulations (using HFSS and Maxwell3D, respectively) with variations of the MBF are presented for several PM configurations. To the best of the authors' knowledge, the only related work for a saturated ferrite disk is presented in [27]. For a fixed standard commercially available ferrite disk, we show that applying different MBF distributions, implemented with various PM configurations, can result in a wide range of performance parameters. Aspects such as operating frequency, bandwidth, matching, insertion loss, and isolation, are analyzed and compared. It is essential to highlight that this study does not intend to demonstrate state-of-the-art circulator performance, but rather to give insights to the designer of how to use available CAD tools and the MFB distribution for achieving specific design parameters.

This article is organized as follows. In Section II, a CAD-based design approach using commercial tools is overviewed. Section III discusses the ferrite effective permeability behavior over magnetic field bias and frequency. In Section IV, the effects on circulator behavior are analyzed when an MBF above saturation is applied. Section V discusses the influence of disk geometry on demagnetization and the effects on the total internal magnetic field. Section VI introduces nontraditional biasing geometries and a study of the distribution of the applied MBF for different PM physical configurations. The theoretical and simulation results are validated in Section VII by measurements of three prototype designs that use the same commercial ferrite disk but operate in three distinct bands around 1.6, 4.3, and 7 GHz.

II. CAD-Based Design Overview

Figs. 1 and 2 show the main geometric parameters of a microstrip ferrite circulator. The ferrite disk is embedded in the PCB substrate on top of the ground plane and is in general thinner than the substrate. Here, we allow different PM geometries, such as the array of small magnets shown in the figures.

Ferrite materials are extensively discussed in the literature (see [28]). The main parameters given for a commercial ferrite material are magnetization saturation ($4\pi M_s$ usually
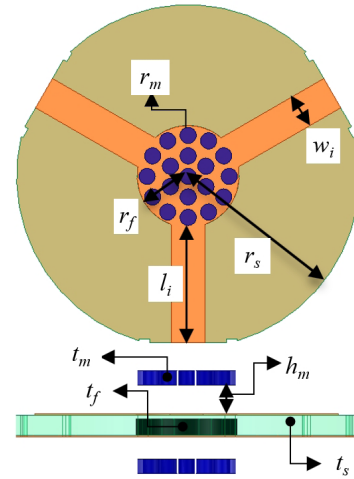

Fig. 2.   Relevant dimensions of a Y-junction microstrip circulator: ferrite radius r_f and thickness t_f, microstrip dielectric substrate thickness t_s, and microstrip line length l_i and width w_i. The magnets have radii r_m and thicknesses t_m and are h_m above and below the copper layers on the two sides of the microstrip substrate.

in Gauss), ferromagnetic resonant frequency (FMR) linewidth (ΔH in oersted), relative permittivity (ϵ_r), and initial relative permeability (μ_r). The parameters that are chosen or determined during the design are the external MBF, internal magnetic field (H_0 in Oe), Larmor or free-precession frequency (f_0), the FMR (f_r), the permeability tensor $[\mu]$, and the effective (scalar) permeability (μ_{eff}).

Fig. 3 shows a simplified flowchart for determining dimensions of a microstrip circulator, for a baseline design that assumes a uniformly saturated ferrite with an operating bandwidth below the FMR. Then, assuming an infinite material, we set FMR $= f_0$ and calculate the resulting internal field as

$$H_0 = f_0/\gamma \qquad (1)$$

where $\gamma = 2.8$ MHz/Oe. Then, we set MBF $= H_0$, giving a saturation magnetization $4\pi M_s = H_0$ in the CGS system of units where $\mu_0 = 1$ and M_s is in gauss. Now, a material can be chosen based on the specified value of M_s, and the FMR linewidth ΔH is then also given. For example, given a center frequency of 3.8 GHz, the calculated FMR$=4.9$ GHz and $M_s = 1750$ G. The Skyworks TTI-105 ferrite material has this value of M_s and losses characterized by $\Delta H = 280$ Oe [29]. The ferrite disk initial dimensions are next calculated from $[\mu]$ and μ_{eff} according to standard equations given in, e.g., [30]. For the given center operating frequency, the FMR is placed about 30% higher, and the disk thickness is chosen to be 10% of its diameter, which is the minimum commercially available thickness.

Now that the radius of the ferrite resonator is determined, we perform EM simulations toward a baseline design of a microstrip circulator, as shown in Fig. 4. A driven full-wave simulation is next performed with a uniform MBF. In HFSS, for instance, we suggest starting with an internal MBF of $\vec{H}_0 = \mu_0 \vec{M}_s$, converted from CGS to SI units. In this simulation, a substrate with a minimum thickness equal to that of the ferrite disk can be used, and the junction geometry (top microstrip metal) is placed immediately above the disk and initially has the same radius. The realistic nonuniform
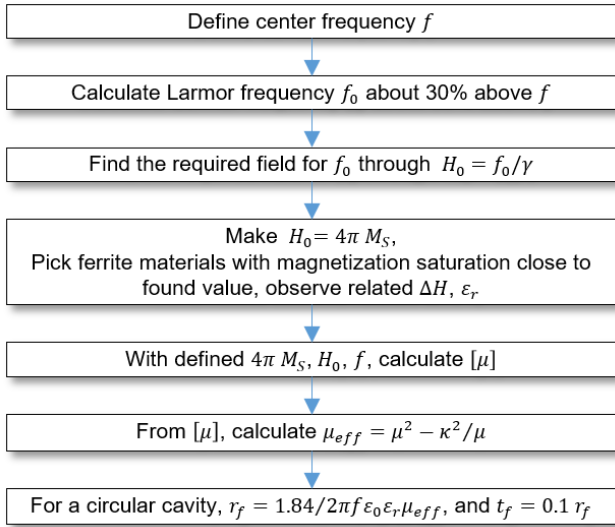
Fig. 3. Procedure for determining dimensions for a circular uniformly saturated ferrite disk, operating below FMR.
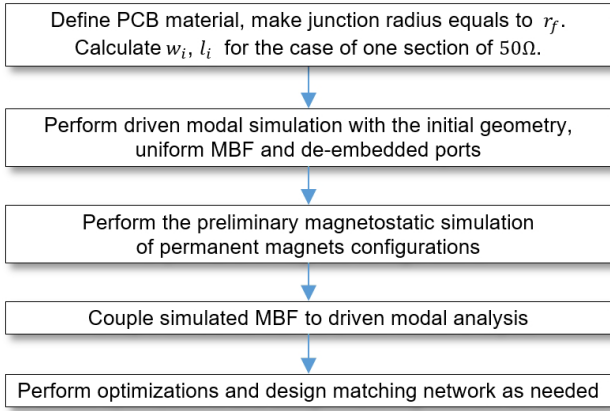

Fig. 4. Steps for full-wave and magnetostatic simulations for microstrip circulators with nonuniform MBF at different levels of saturation resulting from realistic PMs.

MBF is introduced through magnetostatic cosimulations with a tool such as Ansys Maxwell3D. The nonuniformity can result in a frequency shift, increase in insertion loss, and degradation in isolation, requiring design modifications. Additional eigenmode analysis can be performed to evaluate the effect of nonuniform MBF due to demagnetization for different ferrite shapes. Coupled magnetostatic and full-wave RF simulations are useful in the tradeoff between size and performance and will be discussed in detail in Section III. The design is performed with 50-Ω ports and microstrip lines that are deembedded to determine the complex impedance at the edge of the ferrite disk. An impedance-matching network is then designed to trade off return loss, isolation, and bandwidth.

III. FERRITE BEHAVIOR AS A FUNCTION OF THE TOTAL INTERNAL FIELD H_0 AND FREQUENCY f

One way to examine ferrite behavior in the context of a microstrip circulator is first to consider an infinite material approximation and evaluate μ_{eff} as a function of frequency and total internal field. The well-known expression of the scalar complex effective permeability depends on the relationship between the magnetization vector $\vec{M}$, the magnetic flux density $\vec{B}$, and the permeability tensor $[\mu]$

$$\vec{B} = \mu_0(\vec{H} + \vec{M}) = \mu_0(\vec{H} + [\chi]\vec{H}) = [\mu]\vec{H} \quad (2a)$$

$$[\chi] = \begin{bmatrix} \dfrac{f_0 \, f_m}{f_0^2 - f^2} & j\dfrac{f f_m}{f_0^2 - f^2} & 0 \\ -j\dfrac{f f_m}{f_0^2 - f^2} & \dfrac{f_0 \, f_m}{f_0^2 - f^2} & 0 \\ 0 & & 0 \end{bmatrix} \quad (2b)$$

$$[\mu] = \mu_0(I + [\chi]) = \begin{bmatrix} \mu & j\kappa & 0 \\ -j\kappa & \mu & 0 \\ 0 & & \mu_0 \end{bmatrix} \quad (2c)$$

$$\mu_{\text{eff}} = \frac{\mu^2 - \kappa^2}{\mu} \quad (2d)$$

where $[\chi]$ is the susceptibility tensor for an infinite material, f_0 is the Larmor frequency, and f_m is the precession frequency at saturation. When the RF frequency $f = f_0$, the disk is close to resonance (FMR) and all RF power is transferred to the spins [31]. If the material shows no loss, the permeability tensor components experience a singularity at this frequency. However, damping exists and is characterized by ΔH. The loss can be considered when computing the permeability tensor components by defining a complex resonant frequency $\hat{f}_0$

$$\hat{f}_0 = f_0 + j\frac{\Delta H \mu_0 \gamma}{2 f_{\text{FMR},m}} \cdot f \quad (3)$$

where $f_{\text{FMR},m}$ is the frequency where ΔH is measured.

Fig. 5 shows the behavior of $[\mu]$ components and μ_{eff} over frequency for the TTI-105 ferrite material, with $M_s = 1750\,\text{G}$, $\Delta H = 280\,\text{Oe}$, and $f_{\text{FMR},m} = 9.4\,\text{GHz}$. The figure illustrates the regions below and above the FMR for a fixed and uniform $H_0 = 1750\,\text{Oe}$. The singularity points do not reach infinite values since ΔH is different from zero. There is also a 2-GHz shift in the zero crossings of components of $[\mu]$ and μ_{eff}, resulting from the Larmor and FMR frequencies. This plot is useful for design since it points to the frequency ranges that should be avoided to achieve low-loss operation, but it only gives an indication for one fixed value of the MBF.

Off-the-shelf ferrite materials typically have values for M_S in the range 90–5000 G and ΔH from 0.5 to 2500 Oe and can operate between 0.02 and 94 GHz [32]. As shown in Fig. 5, we notice that there is a frequency shift in μ_{eff} relative to the Larmor frequency, and therefore, we study the dependence of the complex μ_{eff} on frequency and H_0 to identify high absorption regions.

An example is shown in Fig. 6 for the TTI-105 material. The real (blue) and imaginary (yellow) effective permeability μ_{eff} is shown over a frequency range $f = [1; 8]\,\text{GHz}$ and for a theoretical internal magnetic field of $H_0 = [1000, 3000]\,\text{Oe}$. The graph clearly shows the low-loss regions above and below the FMR. The 2-D plots illustrate the local behavior with one of the variables fixed. Note that the μ_{eff} approach is restricted to geometries where the RF wave propagation is transverse to the bias, as in the case of a microstrip circulator.

At this point, it is worth clarifying the nomenclature adopted for the regions of operation of a circulator throughout this article; in the circulator industry, a below-resonance circulator operates below FMR and is also referred to as a weakly biased circulator. An above-resonance circulator operates above FMR
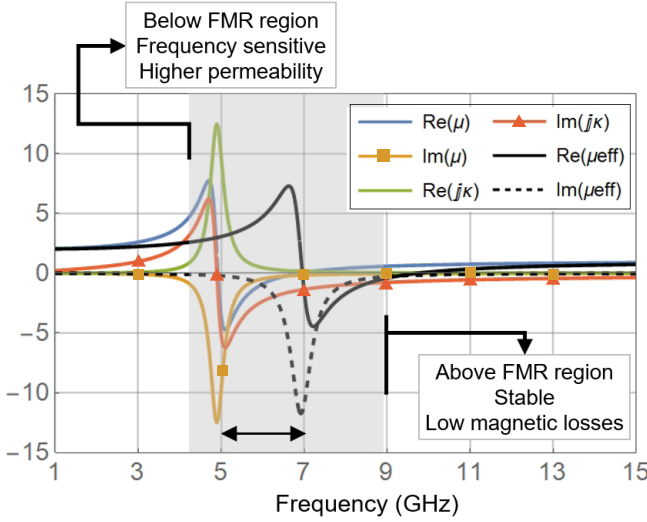
Fig. 5. Real and imaginary parts of κ, μ, and μ_{eff} over frequency for TTI-105 ferrite material parameters. The shaded area indicates the region of high absorption.
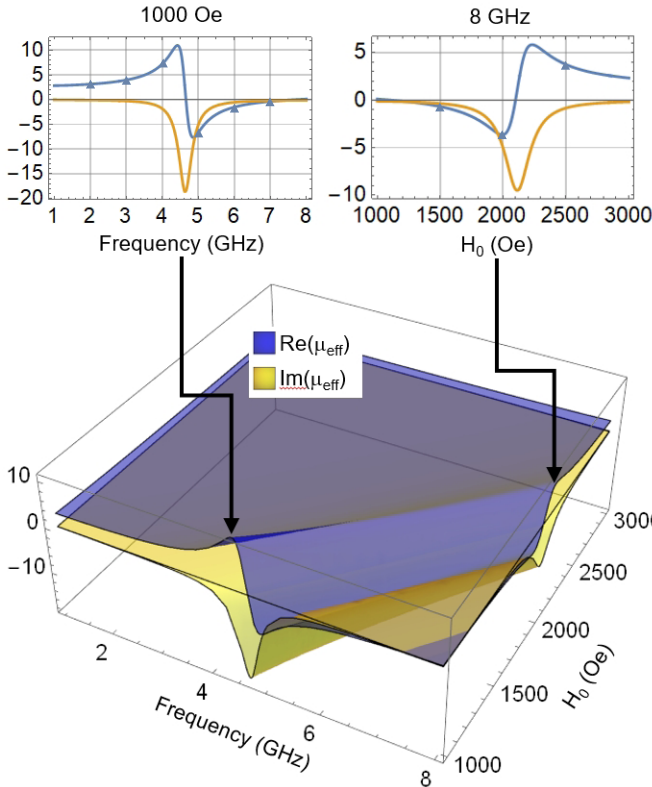

Fig. 6. Simulated real (blue, triangle) and imaginary (yellow) effective relative permeability μ_{eff} for the Skyworks TTI-105 material over a frequency range $f = [1, 8]$ GHz and $H_0 = [1000, 3000]$ Oe. The 2-D graphs in the insets illustrate the local behavior with one of the variables fixed.

and is also referred to as a strongly biased circulator. However, we understand that no matter what the level of magnetization is, an FMR region will occur and it is simultaneously frequency and magnetization dependent, as shown in Fig. 6. Thus, we chose the nomenclature "above" and "below FMR" by splitting the operation regions based on the high loss area in multiparameter space. Even though Fig.6 shows the concurrent dependence of μ_{eff} using Polder's model, the same analysis
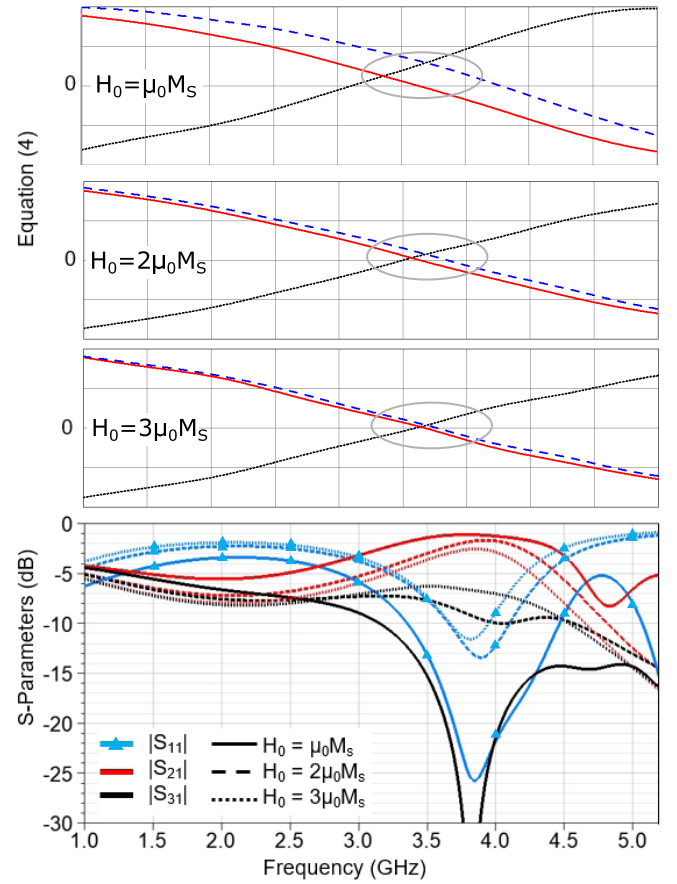

Fig. 7. Resonance analysis for $n = 1$ and $H_0 = \mu_0 M_s$, $2\mu_0 M_s$, and $3\mu_0 M_s$ plotted with S-parameters, showing a relationship between (4) zero crossing, bandwidth, and MBF intensity. Three cases are traced: one considering μ_{eff} as a scalar isotropic quantity (red solid line) and two counter-propagating modes resulting from a tensor $[\mu]$ (dotted and dashed lines). Bottom: S-parameters resulting from the driven analysis for the three cases of the internal field.

can be done by using models for weakly biased ferrites, available in [19], [33], and [34].

IV. EFFECTS OF HIGH-INTENSITY MBF ON CIRCULATOR BANDWIDTH

The effects of MBF with intensities higher than the magnetization saturation are next studied through a comparison between modal analysis and driven simulations. A thin disk is biased with a uniform internal field in the z-direction and has the internal magnetic flux density radial dependence proportional to Bessel functions [4]

$$B_{\pm n} \propto J_n'(k\rho) \pm \frac{n\kappa}{k\rho\mu} J_n(k\rho) \qquad (4)$$

where n is the mode number, $J_n(k\rho)$ is the nth order Bessel function, and k is the wavenumber.

The sum of Bessel functions given in (4) can be plotted as a function of frequency and is shown in Fig. 7. The plot shows resonances (zeros) for $n = \pm 1$ and $H_0 = \mu_0 M_s$, $2\mu_0 M_s$, and $3\mu_0 M_s$. We observe that the zero crossings are closer to the resonances calculated with μ_{eff} (scalar—green line) as the MBF increases. This result is expected since the ratio κ/μ decreases. The corresponding S-parameters are shown at the bottom. Note that the optimum MBF is not the highest
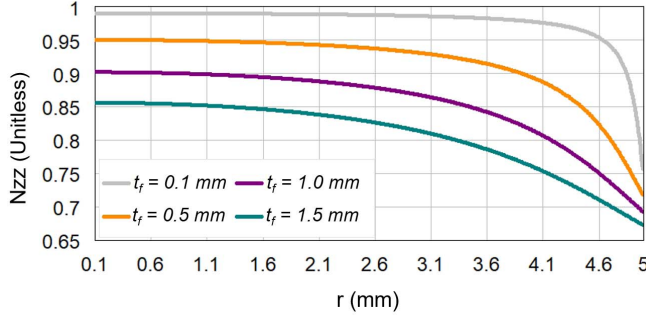
Fig. 8. Demagnetization factor in a cylindrical dielectric magnetic resonator as a function of radius and thickness.
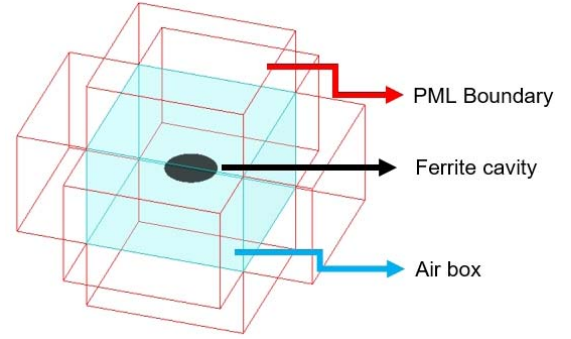

Fig. 9. Geometry for eigenmode simulations showing the empirically determined limits for the air-box ($0.35\lambda_0 \times 0.35\lambda_0 \times 0.25\lambda_0$ at 3.5 GHz) and absorbing boundary condition boxes with the largest dimension of $0.65\lambda_0$.
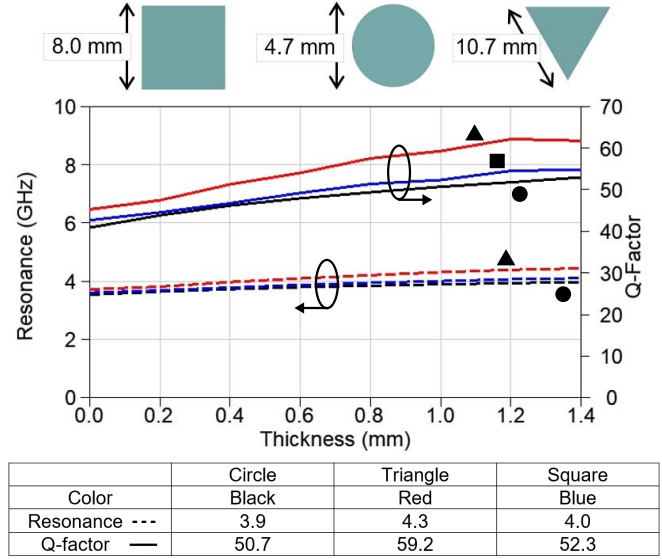

	Circle	Triangle	Square
Color	Black	Red	Blue
Resonance - - -	3.9	4.3	4.0
Q-factor —	50.7	59.2	52.3

Fig. 10. Eigenmode analysis for resonant frequency and unloaded Q-factor for three canonical disk shapes as a function of disk thickness. A scalar μ_{eff} is used in the HFSS simulations, calculated from Skyworks TTI-105 material parameters and with $H_0 = 1750\,\text{Oe}$ at $f = 3.5\,\text{GHz}$. For example, for a thickness of 1.0 mm (table), the circular disk is resonant at 3.9 GHz with a corresponding Q=50.7.

one. In fact, there is a decrease in bandwidth with increasing MBF, indicating that the distance between zero crossings is affected by the bias field magnitude and therefore affects device bandwidth. This can be seen in the driven simulation by observing the S-parameters of the device obtained under the different MBF conditions.

V. EFFECT OF FERRITE GEOMETRY ON DEMAGNETIZATION AND TOTAL INTERNAL FIELD H_0

For a finite ferrite size, boundary conditions must be met at the edges of the disk, resulting in a demagnetizing field that varies within the ferrite volume [22] and changes the magnetization vector. It can be described as a tensor, with components referred to as *demagnetization factors*. The relationship between the demagnetization field and factors is given by

$$\vec{H}_i^{(\text{dem})} = 4\pi \sum_j N_{ij} \vec{M}_j \qquad (5)$$

where i is the component of the demagnetizing field, $\vec{M}_j$ refers to the (ρ, ϕ, z) or (x, y, z) components of the magnetization vector, and N_{ij} are the demagnetization factors. The total internal field H_0 (in Oe) depends on the applied MBF and the demagnetization factors. For a ferrite disk, we assume a z-oriented magnetization of magnitude $M_z = M_s$. For a thin disk, the expression for the internal field is given by [35]

$$H_0 = \text{MBF} - H_i^{\text{dem}}. \qquad (6)$$

To illustrate, the demagnetization for a 5-mm radius cylindrical ferrite is plotted in Fig. 8 as a function of radius and for different thicknesses t_f using equations established in [22]. It shows that thinner cavities exhibit a more uniform demagnetization factor over the cross section, but with a higher magnitude.

The demagnetizing fields change the FMR according to the Kittel relationship [36] causing a drift in frequency

$$\begin{aligned} f_r &= \gamma \sqrt{[H_z + (N_y - N_z)M_z] \times [H_z + (N_x - N_z)M_z]} \\ &= \gamma [H_0 - N_{zz} M_s] \end{aligned}$$

for $N_y = N_x = 0$, $N_z = N_{zz}$, $H_z = H_0$, and $M_z = M_s$.

The effects of thickness variation are addressed by eigenmode simulations. This type of CAD analysis, by its nature, does not include the excitation. For a useful eigenmode analysis, we first calculate the normalized tensor $[\mu]/\mu_0$ at

the center frequency and then assign the values to the μ_{eff} field in the material properties. Perfect electric boundaries are applied on top and bottom faces of the disk. The size of the air-box is a tradeoff between convergence speed and minimum frequency of simulation to avoid overlap with air-box resonances, as shown in Fig. 9. An eigenmode analysis (e.g., in HFSS) can give insight into the behavior of the disk alone.

Fig. 10 shows the result of such an analysis for different ferrite disk shapes, which will result in different demagnetization profiles. The analysis is performed using the relative permeability as a scalar μ_{eff}, calculated from the Skyworks TTI-105 material parameters and $H_0 = 1750\,\text{Oe}$ at $f = 3.5\,\text{GHz}$. The plot shows the resonant frequency and Q-factor for a square, circular, and triangular thin ferrite, as a function of the thickness. As thickness increases, there is an upward shift in frequency, as well as an increase in unloaded Q-factor and it can be explained through the fact that demagnetization factors and phase velocity inside the disk change with geometry. The triangular case shows the most pronounced effect of demagnetization.
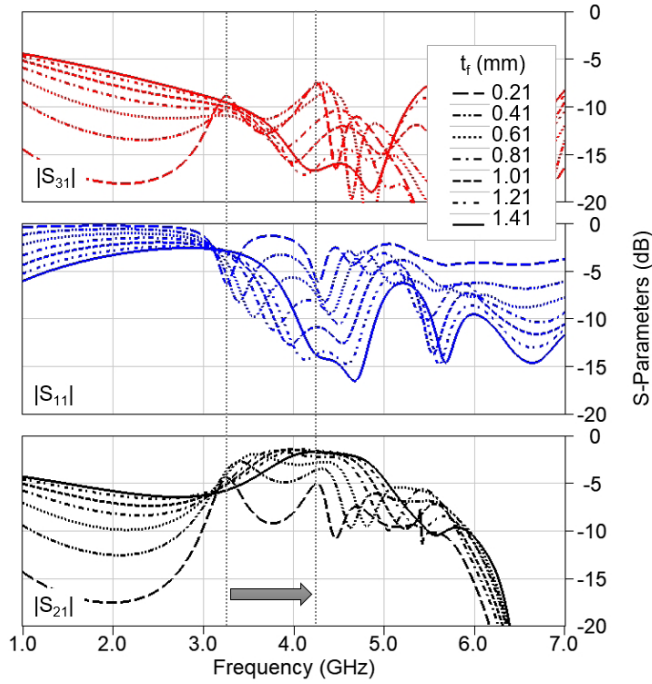
Fig. 11. Parametric-driven simulation for a variation of the disk thickness $t_f = [0.21, 1.41]$ mm. The disk has a circular cross section and is designed from equations given in (4) and (5). Material parameters are defined by Skyworks TTI-105 datasheet biased with an MBF $H_0 = 1750$ Oe. Gray arrow: shift in resonance as thickness increases.

Thickness variations can also substantially change the relationship between dielectric and conductor losses, resulting in frequency shifts and increased insertion loss. Fig. 11 shows the simulation results for a thickness variation of $t_f = [0.21; 1.41]$ mm. A shift to higher frequencies can be observed as thickness increases, agreeing with the results obtained by eigenmode simulations from Fig. 10. Furthermore, an increase in $|S_{21}|$ and improvement in $|S_{31}|$ and $|S_{11}|$ are observed for larger t_f, consistent with the Q-factor increase with larger disk volume.

VI. DISTRIBUTION OF THE APPLIED MBF

The MBF distribution generated by PMs depends on factors, such as grade, shape, and distance from the ferrite disk. This distribution will affect RF performance. For example, Fig. 12 shows the MBF distributions with the change in distance h_m of a pair of cylindrical rare-earth PMs *HKCM* NdFeB-N35 [37] with a thickness $t_m = 3$ mm and diameter $d_m = 18$ mm. The MBF distribution is simulated for two cases: $h_m = 0.01$ and $h_m = 15$ mm. The top of Fig. 12 shows that the total variation of the MBF goes from 260 to 30 kA/m as the PMs are separated. The bottom of the figure shows the magnetic flux density distribution, where the weaker field appears in the center for $h_m = 0.01$ mm, while the intensity is higher in the center for $h_m = 15$ mm.

Next, we consider a different PM distribution in the shape of two arrays of 19 small magnets on the two sides of the junction. In this case, the resulting MBF distribution, obtained by magnetostatic simulations, is shown in Fig. 13. The MBF shows no symmetry and is very nonuniform, and the ferrite is saturated only in a few small isolated parts.
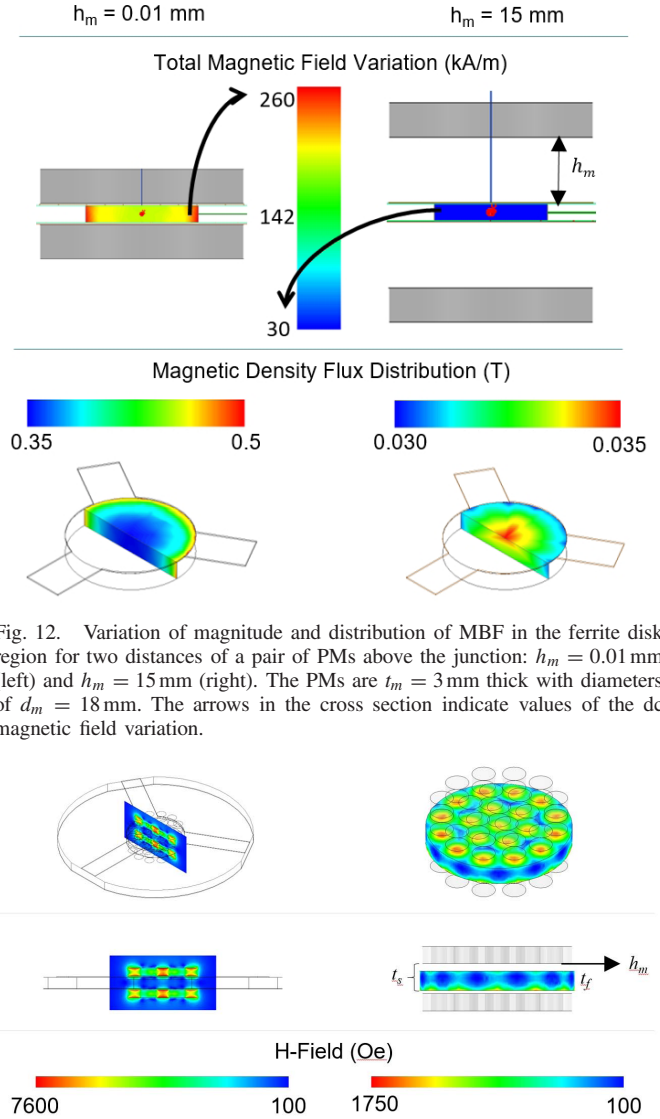

Fig. 12. Variation of magnitude and distribution of MBF in the ferrite disk region for two distances of a pair of PMs above the junction: $h_m = 0.01$ mm (left) and $h_m = 15$ mm (right). The PMs are $t_m = 3$ mm thick with diameters of $d_m = 18$ mm. The arrows in the cross section indicate values of the dc magnetic field variation.
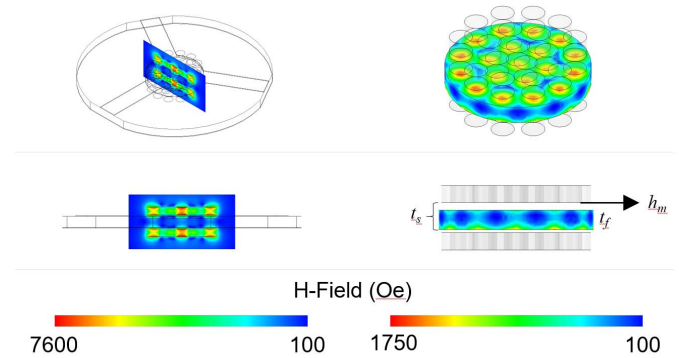

Fig. 13. Simulated MBF generated by an array of 19 N50 grade PMs, concentrically distributed and mirrored in the z-direction around the center plane of the substrate. The dimensions are $t_m = 1.106$ mm, $r_m = 0.79$ mm, $t_f = 1.249$ mm, $t_s = 1.524$ mm, and $h_m = 0.1$ mm. Magnetic field in the xz plane, including the PM volumes (left). The MBF inside the ferrite volume (right).

In Figs. 12 and 13, the simulated magnetostatic field distributions show that the synthesis of a certain MBF is highly dependent on the PM geometries and distance from the ferrite disk. In some cases, it will completely change the internal field distribution and hence impact the magnetization levels at every point in the ferrite.

VII. EXPERIMENTAL VALIDATION

To validate the above analysis experimentally, three circulators using the same ferrite disk are designed, fabricated, and characterized, and their main characteristics are summarized in Table I.

A. Baseline Circulator

Since the applied MBF determines the distribution and level of magnetization inside the ferrite and it can also vary with PM

TABLE I
VALIDATION CIRCULATOR DESIGNS FOR DIFFERENT
OPERATING POINTS USING THE SAME FERRITE DISK

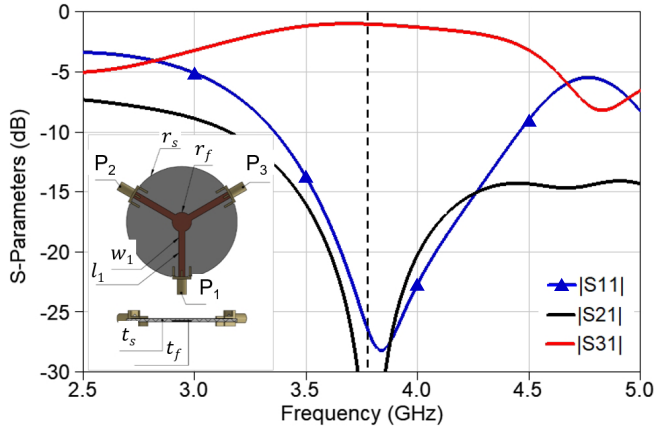| Bias Strategy	f_0 (GHz)	Goal
Unsaturated nonuniform	1.6	Miniaturization
Saturated uniform	4.4	Baseline
Unsaturated nonuniform with array of PMs	7.2	Tuning at frequencies above FMR

Fig. 14. Baseline microstrip junction circulator design, where simulations are performed for a uniform MBF.

geometry and relative position to the ferrite disk, a baseline circulator is first designed for comparison purposes. Using a traditional design approach, a circulator is implemented, as shown in Fig. 14. The disk has a 5-mm radius and is made of TTI-105 ferrite material, the same radius microstrip circular junction, thickness of both ferrite and substrate of $t_s = t_f = 1.524$ mm, substrate dielectric constant $\epsilon_r = 3.6$ (Rogers RO4350C), and microstrip linewidth of 3.5 mm corresponding to 50 Ω.

The performance in Fig. 14 is simulated for a uniform MBF of 1750 G. The measured performance shown in Fig. 15(a) shows a shift in frequency from 3.8 to 4.3 GHz (solid lines). The dashed lines show the simulated results with a nonuniform MBF obtained as in [38]. The implemented circulator is shown in Fig. 15(b) and uses two rare-earth commercially available magnets with a thickness of $t_m = 3$ mm and diameter $d_m = 15.85$ mm, with specifications for the commercially available HKCM NdFeB-N35 material [37].

B. Miniaturized Design Operated Below Saturation

A second variation of the design is studied with an MBF below saturation magnetization to test frequency change. This is accomplished by moving the PMs away from the disk, as shown in Fig. 12. As H_0 decreases, μ_{eff} increases, resulting in electrically smaller cavities. This can be used for miniaturization at the cost of bandwidth reduction. Fig. 16 shows the simulated S-parameters corresponding to $h_m = 15$ mm and with the same ferrite disk size. A frequency shift from 4.3 to 1.6 GHz is observed, resulting in a reduction of electrical size by 63%. A bandwidth reduction from 25% to 10% is also seen, validating the analysis.

The S-parameters in Fig. 16 are plotted for a junction with 50-Ω microstrip lines connected to the ports. In [38],
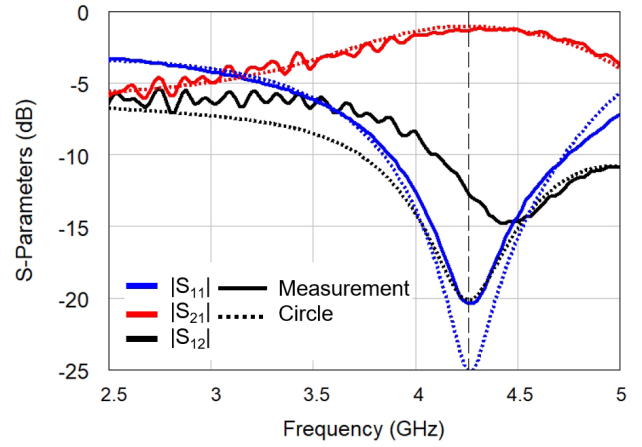
(a)
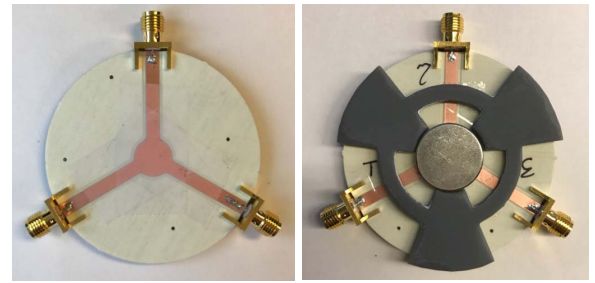
(b)

Fig. 15. (a) Baseline circulator simulated and measured performance of $|S_{11}|$, $|S_{21}|$, and $|S_{12}|$. (b) Photograph of fabricated microstrip circulator, showing the position of the PMs (one on the top, the other not visible below) [38]. The gray magnet holder is made of low-permittivity plastic and does not affect RF behavior.
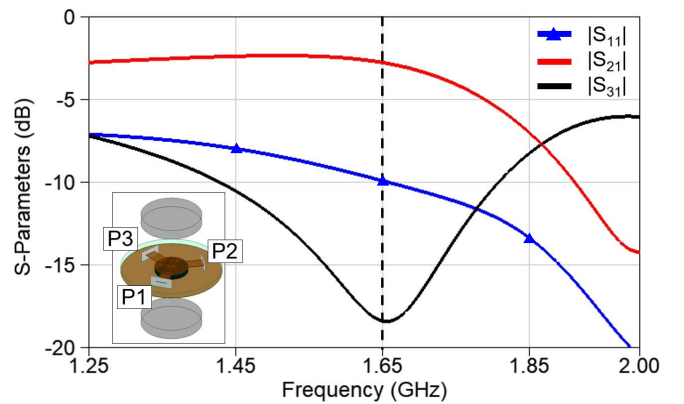

Fig. 16. S-parameters of a microstrip circulator designed to operate at 1.6 GHz. The ferrite disk dimensions are the same as in the previous design, centered at 4.3 GHz. To make the disk electrically smaller, a weaker MBF is applied by displacing the PMs apart.

impedance matching is shown to improve bandwidth, and an example of impedance matching that results in improved simulated and measured isolation and bandwidth is shown in Fig. 17. The microstrip matching network shown in the photograph can easily be designed with surface-mount lumped elements for further size reduction.

C. Design With Nonuniform MBF

To validate the theory related to an extremely nonuniform MBF, another design variation is studied by substituting the
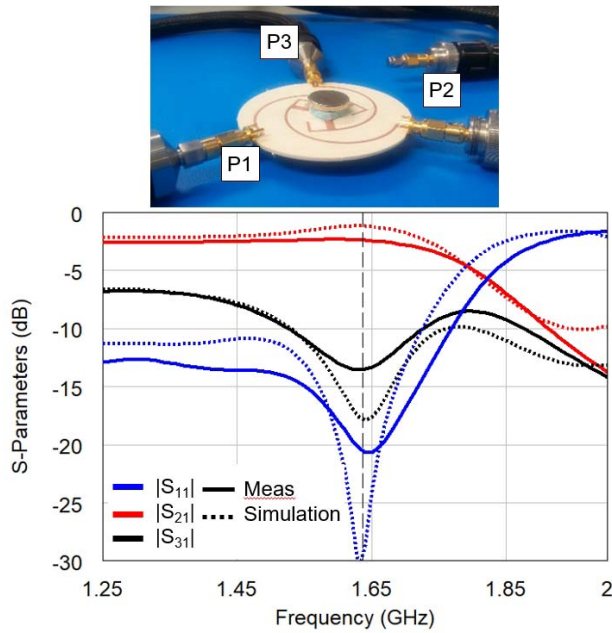
Fig. 17. Circulator operating in the UHF band having a reduced disk size by 40% [38]. The disk is initially designed to operate at 4.4 GHz when the ferrite is uniformly saturated. Foam spacers are used to define the distance from the disk.
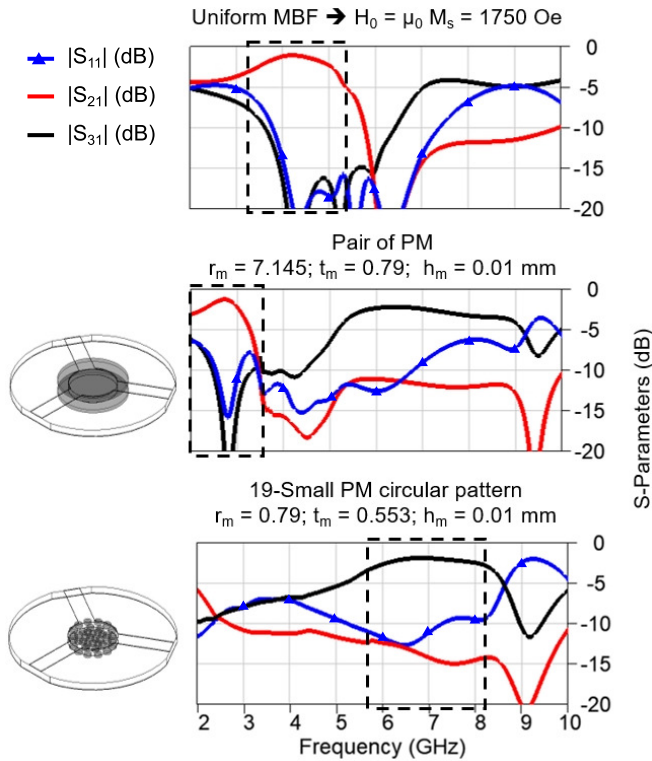

Fig. 18. Simulated S-parameters for different MBF distributions. Uniform MBF of $4\pi M_s = 1750$ G applied directly in HFSS (top), nonuniform MBF obtained through the magnetostatic cosimulations in Maxwell3D of a pair of cylindrical PMs (middle), and array of PMs (bottom). The dashed boxes show the shift in frequency of the operating point as MBF distribution changes. All lines and ports are 50Ω, and the reference planes are deembedded.

traditional pair of big PMs by nonuniform arrays of small magnets (see Fig. 13). The idea is to add a degree of freedom to the design by changing the MBF distribution and isolating the
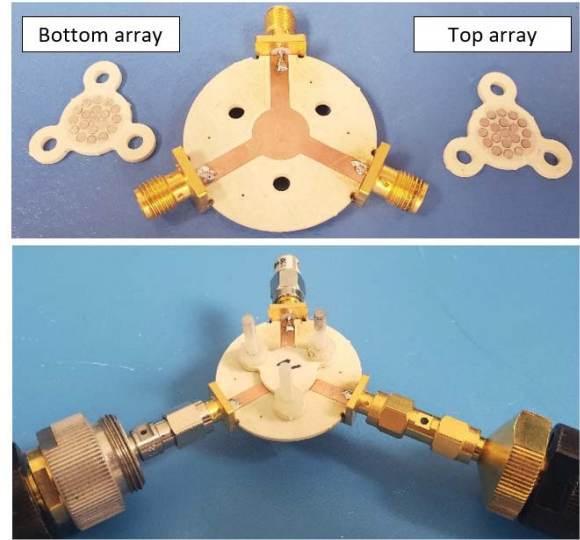

Fig. 19. Photograph of third prototype presented in Fig. 18. The circulator is designed to operate above FMR by applying a nonuniform MBF with an array of small PMs.
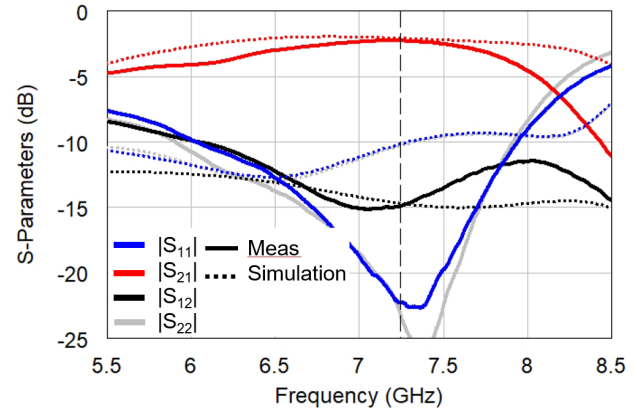

Fig. 20. Simulated and measured S-parameters of the circulator shown in Fig. 19. The measurements were performed with a two-port VNA, so isolation is measured by $|S_{12}|$. At 7.2 GHz, measured parameters are $|S_{11}| = -21.8$ dB, $|S_{21}| = -2.3$ dB, and $|S_{12}| = -15.0$ dB.

effects of matching networks. Fig. 18 shows the S-parameters for the same previous disk for three configurations: an ideal uniform MBF of $4\pi M_s = 1750$ G applied directly in HFSS, nonuniform MBF obtained through the magnetostatic cosimulations in Maxwell3D of a pair of cylindrical PMs, and the different nonuniform MBF generated by an array of small magnets. The two larger PMs are of a grade N50 material with radii $r_m = 7.145$ mm, thicknesses $t_m = 0.79$ mm, and $h_m = 0.1$ mm. Two arrays of 19 magnets in a circular lattice with $r_m = 0.79$ mm, $t_m = 0.553$ mm, and $h_m = 0.1$ mm are placed on the two sides of the microstrip substrate. When the disk has a theoretical uniform MBF, the first mode is dominant and at a frequency associated with the ferrite diameter. When a nonuniform MBF is generated by the two larger PMs, a shift in frequency is observed since a variation in the MBF distribution will change the internal field and, thus, the effective permeability. As in an ordinary dielectric cavity with fixed geometry, if ϵ_r and μ_r change, the resonances in the ferrite disk will drift. When the MBF distribution is modified
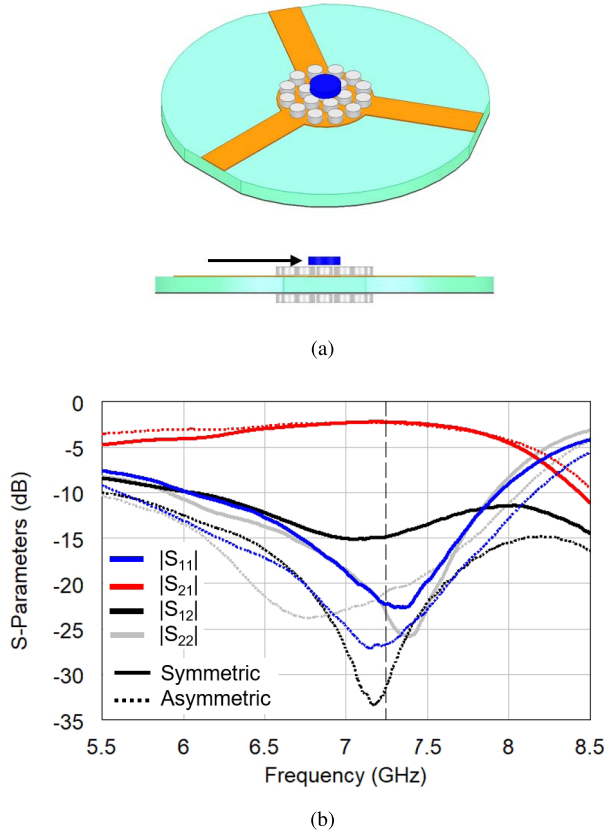
(a)

(b)

Fig. 21. (a) Geometry for an asymmetric 3-D PM configuration and (b) measured S-parameters of initial permanent magnetic array (2-D) and the 3D-asymmetric array.

TABLE II

PERFORMANCE SUMMARY OF CIRCULATORS FROM FIG. 22. BW IS DEFINED BY IL < 3 dB, ISO > 10 dB, AND RL > 10 dB

Bias Strategy	f_0 (GHz)	BW (%)	IL (dB)	ISO (dB)	RL (dB)
Unsaturated, PM pair (Fig.17)	1.6	12.5	2.5	17.5	20
Saturated, PM pair (Fig.15)	4.4	13.6	< 1	20	15
Unsaturated, PM array (Fig.21)	7.2	24.8	2.5	30	25

by an array of small PMs, the operating frequency is shifted above FMR and the direction of circulation flips.

The prototype with small-magnet arrays is shown in Fig. 19. Two pieces made of RO4350C were CNC machined to mechanically support the small magnets. The bottom and top arrays were then aligned as shown in the lower image. Fig. 20 shows the agreement between the simulated and measured S-parameters. As expected, the circulator operates around 7.2 GHz. Although the trend is the same, the measured results show a lower bandwidth than simulated results, and this is attributed to fabrication tolerances.

Further exploration of this novel approach is performed experimentally by varying the PM array geometry. For example, when an additional magnet with $r_{m2} = 2$ mm and $t_{m2} = 0.01$ mm is placed on the top of the small-magnet array, making the MBF asymmetric in the z-direction, the S-parameters improve as shown in Fig. 21. Such a result
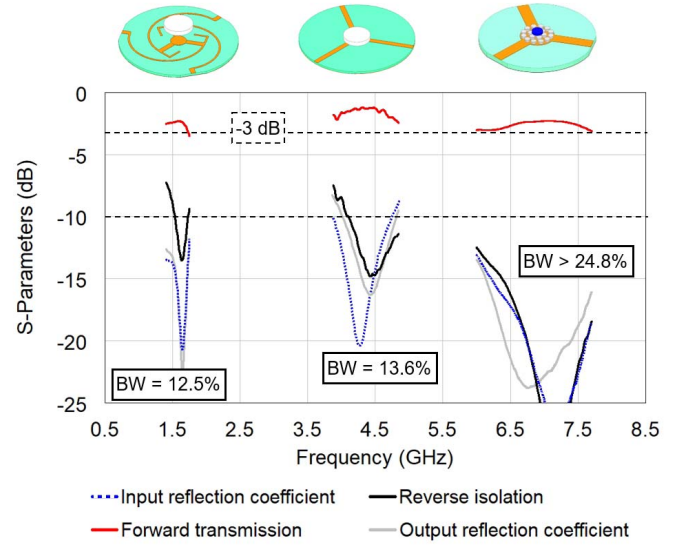

Fig. 22. Summary of measured S-parameters of three microstrip circulators designed with the same ferrite disk. The different frequency bands are a result of different magnetization distributions. The response at the 4.3-GHz center frequency is a result of a design using a nearly uniformly saturated disk, whereas the response at 1.6-GHz center frequency is obtained when the magnetization is nonuniform and below saturation. The 7-GHz response is due to a very inhomogeneous nonsaturated ferrite obtained from an array of PMs.

suggests that the asymmetric structure of a microstrip circulator demands asymmetric MBF for overall compensation.

VIII. CONCLUSION

In summary, this article presents a detailed study of design aspects for microstrip ferrite circulators by controlling the MBF. The approach includes numerical modal analysis, as well as eigenmode and driven simulations to understand the impact of magnetization levels and distribution on circulators' EM performance. A graphical study is developed to characterize the real and imaginary parts of the effective permeability, as a simultaneous function of MBF intensity and frequency. It shows that the low-loss region can be avoided even with a weak MBF. On the other hand, eigenmode analysis combined with driven simulations shows the effects on circulator bandwidth when applied an MBF with higher magnitudes than the ferrite magnetization saturation. The total internal field distribution changes when the same MBF is applied to different ferrite geometries, due to boundary field modification. A parametric study of the resonance and Q-factor of the disk as a function of shape and thickness quantifies this effect, and the results are confirmed with driven full-wave simulations. Finally, the nonuniformity of different PM bias geometries is characterized using magnetostatic and full-wave cosimulations in order to observe the changes in the operation point (above or below FMR), which in turn results in a shift in direction of circulation and frequency.

The analysis is validated using a commercially available ferrite disk (Skyworks TTI-105). The variations on the MBF allows the design of three circulators: a 4.3-GHz device with PMs positioned to produce nearly uniform saturation, a 1.6-GHz device when the same PMs are placed further from the ferrite disk and result in weak biasing, and a 7-GHz device nonuniformly biased with a reduced-volume array of

small magnets. The cosimulations match measured results, which are summarized in Fig. 22 and Table II, showing the greater than two octaves difference in center operating frequencies. Since the impedance at the resonator ports is in general complex, external matching circuits can improve bandwidth but can also be used to introduce other functions such as filtering, as demonstrated in [39].

The two first circulator designs from Fig. 22 are operated below the absorptive FMR region, whereas the third is operated above the FMR with the opposite direction of circulation. The study of designs below FMR is motivated by self-biased circulator constraints, i.e., low volumes, nonuniform, and unsaturated cavities. The same analysis presented here can be applied to investigating circulators with materials characterized by shape anisotropy, e.g., hexaferrites [40] and magnetic nanowires (see [41]). These materials operate below the FMR with no external magnets and have the potential of monolithic integration with active circuits [41].

REFERENCES

[1] J. Helszajn, *The Stripline Circulator: Theory and Practice*. Hoboken, NJ, USA: Wiley, 2008.

[2] D. K. Linkhart, *Microwave Circulator Design*. Norwood, MA, USA: Artech House, 2014.

[3] A. Fox, S. Miller, and M. Weiss, "Behaviour and application of ferrites in the microwave region," *Bell Syst. Tech. J.*, vol. 34, no. 1, pp. 5–103, 1955.

[4] H. Bosma, "On stripline Y-circulation at UHF," *IEEE Trans. Microw. Theory Techn.*, vol. MTT-12, no. 1, pp. 61–72, Jan. 1964.

[5] C. E. Fay and R. L. Comstock, "Operation of the ferrite junction circulator," *IEEE Trans. Microw. Theory Techn.*, vol. 13, no. 1, pp. 15–27, Jan. 1965.

[6] C. M. Krowne, "Cad using green's functions and finite elements and comparison to experimental structures for inhomogeneous microstrip circulators," in *Proc. Adv. Imag. Electron Phys.*, vol. 106. Amsterdam, The Netherlands: Elsevier, 1999, pp. 97–184.

[7] H. Bosma, "On the principle of stripline circulation," *Proc. IEE B, Electron. Commun. Eng.*, vol. 109, no. 21S, pp. 137–146, 1962.

[8] J. B. Davies and P. Cohen, "Theoretical design of symmetrical junction stripline circulators," *IEEE Trans. Microw. Theory Techn.*, vol. MTT-11, no. 6, pp. 506–512, Nov. 1963.

[9] T. Miyoshi and S. Miyauchi, "The design of planar circulators for wideband operation," *IEEE Trans. Microw. Theory Techn.*, vol. MTT-28, no. 3, pp. 210–214, Mar. 1980.

[10] S. Yang, L. Roy, J. R. Bray, and D. Vincent, "Modeling and simulation of a partially-magnetized ferrite LTCC circulator," in *IEEE MTT-S Int. Microw. Symp. Dig.*, Aug. 2015, pp. 1–4.

[11] D. C. Webb, "Design and fabrication of low-cost ferrite circulators," in *Proc. 25th Eur. Microw. Conf.*, vol. 2, Oct. 1995, pp. 1191–1200.

[12] E. F. Schloemann, "Circulators for microwave and millimeter-wave integrated circuits," *Proc. IEEE*, vol. 76, no. 2, pp. 188–200, Feb. 1988.

[13] Y. S. Wu and F. J. Rosenbaum, "Wide-band operation of microstrip circulators," *IEEE Trans. Microw. Theory Techn.*, vol. MTT-22, no. 10, pp. 849–856, Oct. 1974.

[14] J. Young, R. Adams, B. O'Neil, and C. Johnson, "Bandwidth optimization of an integrated microstrip circulator and antenna assembly. 1," *IEEE Antennas Propag. Mag.*, vol. 48, no. 6, pp. 47–56, Dec. 2006.

[15] J. L. Young, R. S. Adams, B. O'Neil, and C. M. Johnson, "Bandwidth optimization of an integrated microstrip circulator and antenna assembly: Part 2," *IEEE Antennas Propag. Mag.*, vol. 49, no. 1, pp. 82–91, Feb. 2007.

[16] T. Jensen, V. Krozer, and C. Kjaergaard, "Realisation of microstrip junction circulator using LTCC technology," *Electron. Lett.*, vol. 47, no. 2, pp. 111–113, Jan. 2011.

[17] H. How *et al.*, "Theory and experiment of thin-film junction circulator," *IEEE Trans. Microw. Theory Techn.*, vol. 46, no. 11, pp. 1645–1653, Nov. 1998.

[18] G. T. Rado, "Theory of the microwave permeability tensor and Faraday effect in nonsaturated ferromagnetic materials," *Phys. Rev.*, vol. 89, no. 2, p. 529, 1953.

[19] E. Schlömann, "Microwave behavior of partially magnetized ferrites," *J. Appl. Phys.*, vol. 41, no. 1, pp. 204–214, Jan. 1970.

[20] J. J. Green and F. Sandy, "Microwave characterization of partially magnetized ferrites," *IEEE Trans. Microw. Theory Techn.*, vol. MTT-22, no. 6, pp. 641–645, Jun. 1974.

[21] E. Schlomann, "On the theory of the ferrite resonance isolator," *IEEE Trans. Microw. Theory Techn.*, vol. MTT-8, no. 2, pp. 199–206, Mar. 1960.

[22] R. I. Joseph and E. Schlömann, "Demagnetizing field in nonellipsoidal bodies," *J. Appl. Phys.*, vol. 36, no. 5, pp. 1579–1593, May 1965.

[23] H. How *et al.*, "Influence of nonuniform magnetic field on a ferrite junction circulator," *IEEE Trans. Microw. Theory Techn.*, vol. 47, no. 10, pp. 1982–1989, Oct. 1999.

[24] A. Guennou, B. Della, P. Qufflec, P. Gelin, and J. L. Mattei, "Influence of the magnetic field nonuniformity on an X-band microstrip Y-junction circulator bandwidth: Theory/experiment comparison," *IEEE Trans. Magn.*, vol. 43, no. 6, pp. 2642–2644, Jun. 2007.

[25] W. Palmer, D. Kirkwood, S. Gross, M. Steer, H. S. Newman, and S. Johnson, "A bright future for integrated magnetics: Magnetic components used in microwave and mm-wave systems, useful materials, and unique functionalities," *IEEE Microw. Mag.*, vol. 20, no. 6, pp. 36–50, Jun. 2019.

[26] V. Laur *et al.*, "Self-biased Y-junction circulators using lanthanum-and cobalt-substituted strontium hexaferrites," *IEEE Trans. Microw. Theory Techn.*, vol. 63, no. 12, pp. 4376–4381, Dec. 2015.

[27] V. V. K Thalakkatukalathil *et al.*, "Electromagnetic modeling of anisotropic ferrites—Application to microstrip Y-junction circulator design," *J. Appl. Phys.*, vol. 123, no. 23, 2018, Art. no. 234503.

[28] Ü. Özgür, Y. Alivov, and H. Morkoç, "Microwave ferrites, part 1: Fundamental properties," *J. Mater. Sci., Mater. Electron.*, vol. 20, no. 9, pp. 789–834, Sep. 2009, doi: 10.1007/s10854-009-9923-2.

[29] *Tt1-105 Parameters*. [Online]. Available: https://www.skyworksinc.com/products/technical-ceramics/tt1-105

[30] R. E. Collin, *Foundations for Microwave Engineering*. Hoboken, NJ, USA: Wiley, 2007.

[31] B. Lax and K. J. Button, *Microwave Ferrites and Ferrimagnetics*. New York, NY, USA: McGraw-Hill, 1962, pp. 149–159.

[32] V. Voronkov, "Microwave ferrites: The present and the future," *Le J. de Phys. IV*, vol. 7, no. C1, pp. C1-35–C1-38, Mar. 1997.

[33] J. J. Green, C. Patton, and F. Sandy, "Microwave properties of partially magnetized ferrites," Raytheon Co Waltham Ma Research Div, Waltham, MA, USA, Tech. Rep., 1968. [Online]. Available: https://scholar.google.com/scholar?hl=en&as_sdt=0%2C6&q=microwave+properties+partially+magnetized+ferrites&oq=microwave+properties+of+partially+raytheon

[34] E. Schlömann, "Behavior of ferrites in the microwave frequency range," *Le J. de Phys. Colloques*, vol. 32, no. C1, pp. C1-443–C1-451, Feb. 1971.

[35] B. K. O'Neil and J. L. Young, "Experimental investigation of a self-biased microstrip circulator," *IEEE Trans. Microw. Theory Techn.*, vol. 57, no. 7, pp. 1669–1674, Jul. 2009.

[36] C. Kittel, "On the theory of ferromagnetic resonance absorption," *Phys. Rev.*, vol. 73, no. 2, pp. 155–161, Jan. 1948, doi: 10.1103/PhysRev.73.155.

[37] *H. Engineering*. [Online]. Available: https://www.hkcm.de/desk.php/

[38] M. Pinto, L. Marzall, A. Ashley, D. Psychogiou, and Z. Popović, "Design-oriented modelling of microstrip ferrite circulators," in *Proc. 48th Eur. Microw. Conf. (EuMC)*, Sep. 2018, pp. 215–218.

[39] A. Ashley, L. F. Marzall, Z. Popovic, and D. Psychogiou, "Frequency selective ferrite circulators with quasi-elliptic transmission response," in *Proc. 48th Eur. Microw. Conf. (EuMC)*, Sep. 2018, pp. 211–214.

[40] V. G. Harris, "Modern microwave ferrites," *IEEE Trans. Magn.*, vol. 48, no. 3, pp. 1075–1104, Mar. 2012.

[41] Y. Cui *et al.*, "Monolithic integration of self-biased *C*-band circulator on SiC substrate for GaN MMIC applications," *IEEE Electron Device Lett.*, vol. 40, no. 8, pp. 1249–1252, Aug. 2019.